

Journal of Materials Chemistry A

Accepted Manuscript



This is an *Accepted Manuscript*, which has been through the Royal Society of Chemistry peer review process and has been accepted for publication.

Accepted Manuscripts are published online shortly after acceptance, before technical editing, formatting and proof reading. Using this free service, authors can make their results available to the community, in citable form, before we publish the edited article. We will replace this *Accepted Manuscript* with the edited and formatted *Advance Article* as soon as it is available.

You can find more information about *Accepted Manuscripts* in the [Information for Authors](#).

Please note that technical editing may introduce minor changes to the text and/or graphics, which may alter content. The journal's standard [Terms & Conditions](#) and the [Ethical guidelines](#) still apply. In no event shall the Royal Society of Chemistry be held responsible for any errors or omissions in this *Accepted Manuscript* or any consequences arising from the use of any information it contains.

Towards accurate prediction of catalytic activity in IrO₂ nanoclusters *via* first principles-based variable charge force field

Fatih G. Sen,¹ Alper Kinaci,¹ Badri Narayanan,¹ Stephen K. Gray,^{1,3} Michael J. Davis,²
Subramanian K.R.S. Sankaranarayanan,^{1,3} Maria K.Y. Chan^{1,3}

¹Center for Nanoscale Materials, Argonne National Laboratory, 9700 S. Cass Ave., Lemont, IL 60439 USA

²Chemical Sciences Division, Argonne National Laboratory, 9700 S. Cass Ave., Lemont, IL 60439 USA

³Computation Institute, the University of Chicago, 5735 S. Ellis Ave., Chicago, IL 60637 USA

ABSTRACT

IrO₂ is one of the most efficient electrocatalysts for the oxygen evolution reaction (OER), and also has other applications such as in pH sensors. Atomistic modeling of IrO₂ is critical for understanding the structure, chemistry, and nanoscale dynamics of IrO₂ in these applications. Such modeling has remained elusive due to the lack of an empirical force field (EFF) for IrO₂. We introduce a first-principles-based EFF that couples the Morse (MS) potential with a variable charge equilibration method, QEq. The EFF parameters are optimized using a genetic algorithm (GA) on a density functional theory (DFT)-based training set. The resultant Morse plus QEq EFF, “MS-Q” in short, successfully reproduces the lattice constants, elastic constants, binding energies, and internal coordinates of various polymorphs of IrO₂ from DFT calculations. More importantly, it accurately captures key metrics for evaluating structural and chemical properties of catalysts such as surface energetics, equilibrium shape, electrostatic charges, oxygen vacancy formation energies, relative stability of low index rutile IrO₂ surfaces, and pressure-induced phase transformations. The MS-Q EFF is used to predict the oxygen binding energy (E_{ad}), a well-known descriptor for OER activity, on various sites of a nanocatalyst. We find E_{ad} to be more favorable at low coordination sites, i.e. edges and corners, compared to planar facets; E_{ad} is also correlated with charge transfer between the adsorbed O and nanocrystal, highlighting the importance of variable charge electrostatics in modeling catalysis on metal oxide surfaces. Our variable charge force field offers encouraging prospects for carrying out large-scale reactive simulations to evaluate catalytic performance of IrO₂ surfaces and nanostructures.

KEYWORDS: Iridium oxide, IrO₂, catalyst, molecular dynamics, force field, vacancy, oxygen adsorption, genetic algorithm, first principles density functional theory

1. Introduction

Iridium oxide (IrO₂) has a number of remarkable properties: it has good electrical conductivity, exceptional chemical and thermal stability,¹⁻⁴ and exciting spintronic⁵⁻⁷ properties; it exhibits the highest formal oxidation state of +9 among all materials⁸; the high chemical stability, conductivity, and near-Nernstian relation to variation in pH, allows IrO₂ to be one of the most efficient pH sensors.⁹⁻¹¹ Most importantly, IrO₂ nanoparticles are also known to be effective electrocatalysts for the oxygen evolution reaction (OER)^{3, 12-15} in electrolysis and photocatalysis¹⁶. Generation of hydrogen fuel from sunlight *via* the photocatalytic water splitting process is one promising route to sustainable energy production.¹⁷⁻²²

The size, shape, and atomic structure of IrO₂ nanoparticles²³⁻²⁹ and nanorods^{28, 30} influence their catalytic, chemical,²³⁻²⁹ and field emission properties.^{28, 30} IrO₂ nanoparticles of technological relevance generally have a diameter in the 1-5 nm range,^{3, 12-14} and consist of different surface atomic structures, facets and defects. The catalytic activity of IrO₂ was reported to depend on the surface orientation, due to differences in the density of coordinatively under saturated metal sites on each facet.³¹ Similar strong correlations between local coordination and catalytic activity of transition metals was previously suggested.³² Also, a recent study by Calle-Vallejo *et al.*³³ generalized the adsorptive scaling relations to include the local atomic environment of the adsorption site for transition metal catalysts. More importantly, density functional theory (DFT) calculations reported that OER and water splitting activity is related to the binding energy of atomic oxygen on rutile oxide surfaces.³⁴ Accordingly, the surface structure and defects play a crucial role in the physical, chemical and thermodynamic properties of IrO₂ in various applications. It is therefore important to accurately predict surface structures, chemistry, and binding energetics to elucidate the atomistic mechanisms in catalytic and other applications.

Atomistic studies of IrO₂ structures are essential for developing an understanding of the physical and chemical properties displayed by different IrO₂ phases and surfaces. Previous DFT studies reported on the

bulk structural, electronic,³⁵⁻³⁷ and surface properties^{34, 38} of IrO₂. Zhou *et. al.*²³ investigated the relative stabilities of Ir_mO_n ($m = 1$ to 5 , $n = 1$ to $2m$) nanoclusters using DFT calculations with the B3LYP hybrid functional and reported on the hydrolysis reaction on nanoclusters. All of the existing atomistic simulations for IrO₂ considered either bulk periodic systems or small clusters. Despite the advances in computing resources, DFT calculations on IrO₂ nanostructures of practical sizes (>2 nm diameter) are still computationally very expensive. Atomistic simulations using empirical force fields, however, are computationally several orders of magnitude more efficient, as well as scalable to span the 2-100 nm diameter range for which nanosize effects are pertinent. The current complete lack of an available force field for the Ir-O system has, however, made studying structure and dynamics in large-scale Ir-O catalysts difficult or impossible.

In the present study, we develop a first principles based empirical interatomic potential or force field that can accurately predict both bulk and surface properties of IrO₂. To capture both the pair and electrostatic interactions, we couple a Morse-type interatomic potential with environment-dependent electrostatic interactions. Electrostatic contributions can be obtained by determining the charge distribution on atoms. Charge distribution on atoms not only contributes to the binding energy, but also influences the atomic interactions between different species, hence affecting the molecular reactivity. Some previous force field models allocate fixed charges on atoms, e.g. Matsui-Akoagi,³⁹ AMBER,⁴⁰ and CHARMM,⁴¹ which renders them incapable of modeling diverse structural environments and chemical reactions. To circumvent this issue, more accurate methods have been recently employed to assign charges dynamically depending on the local environment *via* equalization of the electronegativity. Some of these methods are: electron equalization method (EEM),⁴² charge equilibration method (QEq),⁴³ chemical potential equalization method (CPE),⁴⁴ fluctuation charge model (FQ),⁴⁵ and split-charge equilibration method (SQE).⁴⁶ These methods have a common theme: by allowing the charges to be variable and environment dependent, these can in principle capture bond formation and bond breakage events within the framework of classical MD.⁴⁶ QEq and EEM models have previously enabled accurate prediction of bulk and surface properties of metal oxides when combined with other pairwise interatomic

interactions.⁴⁷⁻⁵⁰ For example, a Morse+QEq (MS-Q) force field for titanium oxide, developed by Swamy and Gale, accurately predicted the bulk moduli and binding energies of various titanium oxide polymorphs, when compared to quantum mechanical calculations, but could not predict the relative surface stability in rutile TiO₂.^{48, 51} There are several possibilities for this shortcoming: the lack of surface energies in the training set,⁵¹ the lack of parametrizing of QEq parameters, and/or the lack of adequate global parameter space search. We hypothesize that it is possible to successfully use MS-Q to describe the IrO₂ system by addressing these missing elements.

Our approach for developing a MS-Q force-field incorporates several key elements: the inclusion of diverse local environments in an elaborate DFT training set that includes surfaces, the parameterization of QEq parameters, and the use of an evolutionary algorithm to parameterize MS-Q. The use of different local environments including broken bonds in the training set enhances the probability that chemical reactions can be modeled with the resultant force field. The QEq parameters, namely, electronegativity and chemical hardness, may depend on chemical environments and therefore should not be expected to be universal for each element. Evolutionary algorithms, particularly genetic algorithms, are proven to be robust and effective methods for parameter search, which can solve problems involving intractably large and complex search spaces and multiple conflicting objectives.⁵²⁻⁵⁴

Our variable charge MS-Q force field for the Ir-O system is parameterized to predict both the structural and surface properties of solid IrO₂. The force field is trained on the results of first principles DFT calculations on IrO₂ bulk phases and surfaces. We use a genetic algorithm to accurately fit the MS-Q parameters to the DFT results. We perform a rigorous test of the developed force field by comparing the bulk, surface and defect properties, and pressure-induced phase transformations of IrO₂ to the corresponding DFT results. Finally, we compute the oxygen atom binding energy, a quantity that has been found to be a useful descriptor for OER activity³⁴ on the surface of an IrO₂ nanoparticle, in order to evaluate the effectiveness of different sites in the catalytic process.

2. Computational Methodology

2.1 DFT calculations

As a first step towards parametrizing the variable force field, an extensive training set is generated. The structural, mechanical, surface, and thermodynamic properties for various experimental and hypothetical crystal structures of IrO₂ are computed using density functional theory (DFT). All DFT calculations are performed using the projector-augmented wave (PAW) method, as implemented in the Vienna Ab-initio Simulation Package (VASP),^{55, 56} and with the generalized gradient approximation (GGA) of the exchange correlation described by Perdew, Burke, and Ernzerhof (PBE).⁵⁷ Calculations are carried out using PAW–PBE atomic pseudopotentials supplied with the VASP code,^{58, 59} and include the Hubbard U correction^{60, 61} which is beneficial for describing unfilled d -shells, and spin orbit coupling (SOC) because SOC effects are substantial for Ir.^{5, 7}

For bulk structures, atomic positions and cell parameters are relaxed. Only atomic positions are relaxed for the surface structures. The calculations are performed with 10×10×10 and 10×10×1 Γ -centered k-point grid for bulk and surface structures, respectively, and a kinetic energy cutoff of 520 eV. These k-point and energy cutoff settings ensure total energy convergence to 1-2 meV/atom.

We determine the Hubbard U parameter used in DFT calculations in order to accurately model the rutile IrO₂ phase, in terms of thermodynamics as well as fundamental electronic structure properties. For thermodynamics, we compare the binding energy (E_b) for the rutile IrO₂, calculated with DFT (Equation 1), to the corresponding experimental value, derived from the formation enthalpy (ΔH_f) of IrO₂⁶²⁻⁶⁶ and the cohesive energies of metallic Ir and the O₂ molecule (Equation 2).

$$E_{b,DFT}(\text{Ir}_n\text{O}_m) = E_{DFT}(\text{Ir}_n\text{O}_m) - nE_{DFT}(\text{Ir}) - mE_{DFT}(\text{O}) \quad (1)$$

$$E_{b,exp}(\text{IrO}_2) = \Delta H_f(\text{IrO}_2) - E_{coh}(\text{Ir}_{metal}) - E_{coh}(\text{O}_2) \quad (2)$$

In Equation 1, $E_{DFT}(\text{Ir}_n\text{O}_m)$ is the total energy of a structure that has n Ir and m O atoms ($n=2$ and $m=4$ for the rutile unit cell), and $E_{DFT}(\text{Ir})$ and $E_{DFT}(\text{O})$ are DFT total energies of the isolated Ir and O atoms, respectively, approximated by a calculation of the single atom in a large (15 Å × 15 Å × 15 Å) box that is repeated periodically. We choose to focus on binding energies referenced to isolated atoms because (1)

the energy obtained from a force field is defined to be zero at the limit where all atoms are infinitely apart from each other, so E_b directly correspond to the energy obtained from the empirical force field, and (2) the energy of the O_2 molecule is known to be problematic in DFT-PBE^{67, 68} (and references therein). The experimental values of ΔH^f range from -2.48 to -2.84 eV/IrO₂,⁶²⁻⁶⁶ which combined with cohesive energies of 6.94 eV/atom for metallic Ir⁶⁹ and 2.60 eV/atom for molecular O₂⁶⁹ give experimental binding energies in the range -14.96 to -14.62 eV/IrO₂. To reproduce these binding energies, Hubbard U values of 1.4 – 1.8 eV are required. However, U values of 1.3 eV or above result in an electronic insulator rather than metal,⁷ in contrary to experimental evidence.⁷⁰ The U value of 1.0 eV is therefore chosen to produce a reasonable binding energy (-15.33 eV/IrO₂) as well as maintain realistic electronic structure properties, for rutile IrO₂. We note also that the U correction is applied only on Ir in IrO₂ but not in metallic Ir, since the cohesive energy of metallic Ir is adequately captured with PBE without a U correction (7.00 eV/atom vs. experimental value of 6.94 eV/atom).

2.2 Training data

The DFT training set includes calculated binding energies ($E_{b,DFT}$, as defined in Equation (1)), lattice parameters, internal coordinates and elastic constants of several IrO₂ structures as shown in Figure 1, including the ground state rutile ($P4_2/mnm$) structure (Figure 1a)⁷¹ and high pressure (>15 GPa) pyrite ($Pa-3$) phase (Figure 1b).⁷² In addition to these experimental structures, we also consider hypothetical anatase ($I41/amd$) (Figure 1c), columbite ($Pbcn$) (Figure 1d) and brookite ($Pbca$) (Figure 1e) polymorphs of IrO₂. Surface energies of (110) and (100) surfaces of rutile IrO₂ are also included in the training set. The use of different polymorphs and two surfaces in the training set provides a variety of local environments in order to capture variable charge effects in the fitted force field.

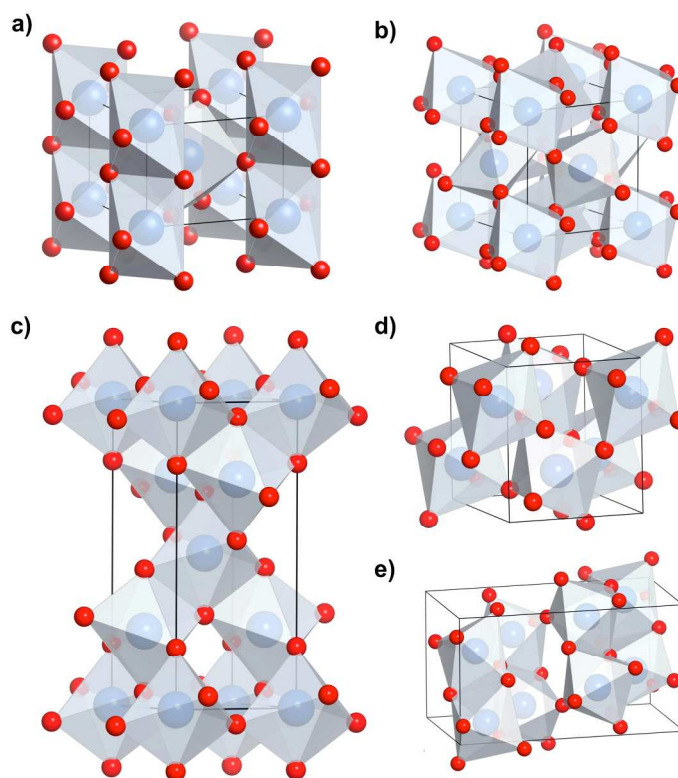


Figure 1. Atomic structure of IrO_2 polymorphs. a) rutile, b) pyrite, c) anatase, d) columbite, and e) brookite.

2.3 Morse+QEq (MS-Q) empirical force field

The empirical force field (MS-Q) is a Morse function coupled with a variable charge electrostatic term utilizing the Charge Equilibration method (QEq).⁴³ The MS-Q force field is used as implemented in General Utility Lattice Program (GULP)⁷³ a molecular dynamics program for materials simulations, and is given by

$$V(r_{ij}) = D_e \left(\left[1 - \exp(-\alpha(r_{ij} - r_0)) \right]^2 - 1 \right) + \frac{q_i q_j}{r_{ij}} \quad (3)$$

The parameter D_e is the bond dissociation energy, α is related to the curvature at the potential minimum (force constant), and r_0 is the equilibrium interatomic distance. The charge on atom i is given by q_i , and is determined in QEq, using the electronegativity (χ), atomic hardness (J), and covalent radius (R) values for Ir and O,⁴³ based on the equalization of the electronegativity. In QEq, the electrostatic self-energy of an ion i is defined as:

$$E_i(q_i) = E_i(0) + \chi_i q_i + \frac{1}{2} J_i q_i^2 \quad (4)$$

where $E_i(0)$ is the self-energy of an ion i . To estimate the charge interactions, the screened Coulomb potential is calculated by describing the atomic density with s-like Slater orbitals, namely $\phi_{n\zeta}^{\text{slater}} = N_n r^{n-1} e^{-\zeta r}$, where n is the principal quantum number and N_n is a normalization constant. The valence orbital exponent ζ is defined as $\zeta = (2n+1)/4R$. A set of χ , J and R parameters are supplied by Rappe and Goddard,⁴³ but we consider them as variable, and parametrize according to our training data set. The Morse portion of the potential is subject to a cutoff distance of 15.0 Å, which is sufficiently large for including long-range interactions.

2.4 Genetic algorithm optimization of force field parameters

An efficient global optimization scheme is necessary to search the 15-dimensional parameter space for an optimal set of parameters, *i.e.* Morse potential parameters D_e , α , and r_0 for Ir-Ir, Ir-O and O-O pairs and QEq parameters χ , J , and R for Ir and O, which best reproduces DFT training data which includes structural, mechanical, and thermodynamic properties. We use the genetic algorithm (GA) approach which has been shown to be effective in global minima search by simultaneously exploring various regions of interest using different members of the population.⁵⁴ The flowchart for the GA parameter optimization process is given in Figure 2. Initially, we randomly assign a number of parameter sets based on the given population size of 100. For each set of parameters, and for each atomic structure in the training set, we evaluate the binding energies of IrO₂ polymorphs at different volumes, the elastic constants and surface energies of the rutile phase, and the lattice parameters and internal coordinates of IrO₂ polymorphs. The calculated observables are compared with the DFT values to determine the weighted sum of squares of errors (ε), with weights w_i determined such that both surface and bulk properties are predicted accurately. The weights used are as follows: energies in eV (typical range: -14.5 to -15.5 eV) have $w_i = 1.0$, elastic constants in GPa (typical range: 100 – 600 GPa) have $w_i = 0.01$, lattice constants in angstrom (typical range: 3 – 10 Å) have $w_i = 100.0$, dimensionless fractional internal

coordinates (0 – 1) have $w_i = 1000.0$, and surface energies in J/m^2 (typical range: 1 – 2.5 J/m^2) have $w_i = 100.0$. A weighting of $w_i = 1000.0$ for the relative polymorph binding energies (in eV) and relative surface energies (in J/m^2) is also included to accurately predict the relative phase stability of IrO_2 polymorphs and the relative surface stability.

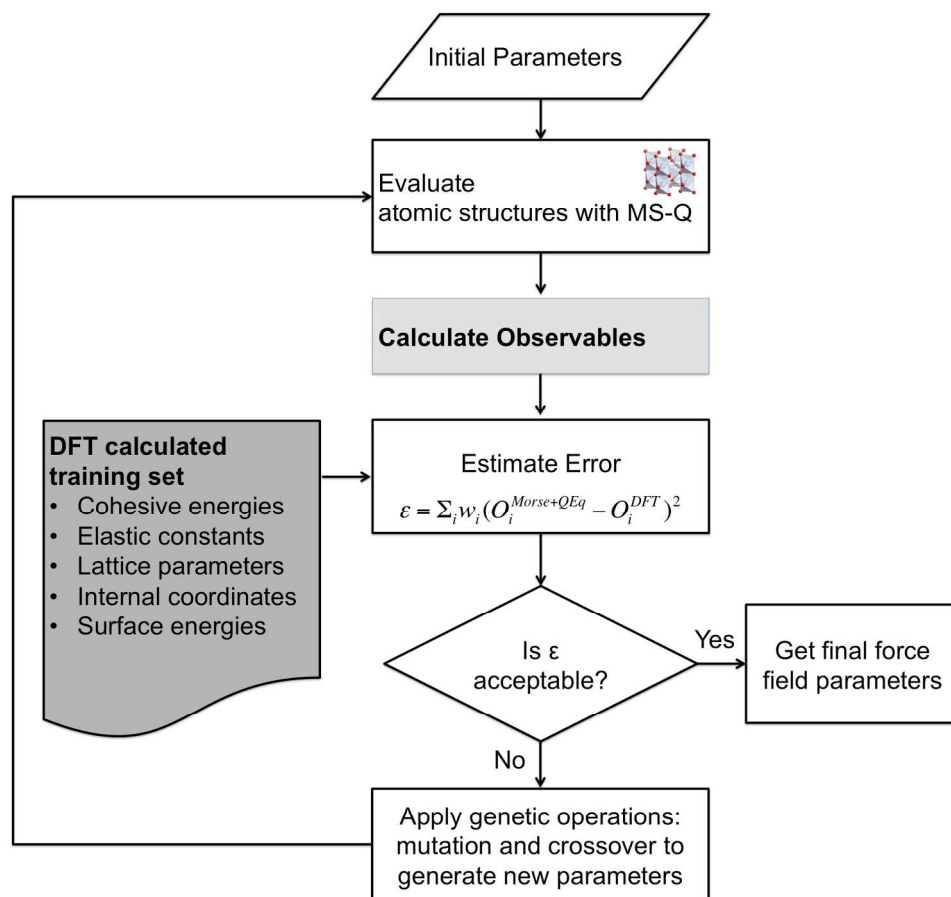


Figure 2. Flowchart for the force field fitting process using genetic algorithm.

At each generation, we perform genetic operations on the parameters, namely tournament selection without replacement,^{74, 75} simulated binary crossover,^{76, 77} and polynomial type mutation of order 20,^{76, 77} to generate a new population of parameter sets. At each generation, a local minimization of ε with respect to the parameter space is carried out using the Simplex algorithm. The fitting process proceeds until the value of ε is converged, *i.e.* experiences less than 1% change for 20 consecutive generations. Each 15 parameter is searched within a physically reasonable range. The ranges for the parameters were $D_e^{\text{Ir-Ir}}$: 0.001 – 0.01 eV, $\alpha^{\text{Ir-Ir}}$: 1.0 – 2.0 \AA^{-1} , $r_0^{\text{Ir-Ir}}$: 3.5 – 6.0 \AA , $D_e^{\text{Ir-O}}$: 1.0 – 3.0 eV, $\alpha^{\text{Ir-O}}$: 1.7 – 3.5 \AA^{-1} , $r_0^{\text{Ir-O}}$: 1.8 –

2.0 Å, D_e^{O-O} : 0.01 – 0.1 eV, α^{O-O} : 1.0 – 2.0 Å⁻¹, r_0^{O-O} : 3.0 – 5.0 Å, χ^{Ir} : 2.0 – 6.0 eV, J^{Ir} : 4.0 – 12.0 eV, R^{Ir} : 1.2 – 1.5 Å, χ^O : 8.0 – 11.0 eV, J^O : 11.0 – 14.4 eV, R^O : 0.6 – 0.7 Å. The fitting process is carried out using the GA Toolbox.⁷⁸ We use a population size of 100, crossover probability of 0.9, and mutation probability of 0.1.

2.5 Evaluation data to test MS-Q

To evaluate the accuracy and transferability of the MS-Q force-field fitted with the GA described above, we perform further DFT calculations to evaluate properties that are not included in the training data. The electronic charges on atoms in DFT calculations are obtained by partitioning the charge density according to atomic positions in the crystal based on the Bader charge analysis.^{79, 80} The Bader charges are compared to QEq charges to determine the correspondence between first principles determined and QEq charges. To understand the thermal and elastic properties as described by the MS-Q EFF, we calculate the phonon dispersion with both DFT and MS-Q. To more rigorously test the transferability of the potential in predicting defective structures, we calculate the Ir and O vacancy formation energies and compare to the DFT results. The pressure-induced phase transformation of IrO₂ polymorphs are calculated with both DFT and MS-Q and compared. Finally, oxygen atom adsorption energetics on rutile (110) surface are computed with MS-Q and the results are compared to DFT values.

3. Results and Discussion

3.1 Fitted parameters and goodness-of-fit

The Morse and QEq parameters obtained from the fitting procedure discussed above are given in Table 1 and Table 2, respectively. The resulting Morse parameter set in Table 1 is physically reasonable in the sense that the largest dissociation energy (D_e) and potential well curvature (α) terms are obtained for the Ir-O pair. The Ir-Ir Morse potential has the weakest interaction and the longest equilibrium bond distance. It should be noted that r_0 for the Ir-O pair is smaller than the Ir-O nearest neighbor distance of 2.01 Å in the thermodynamically stable rutile phase, which ensures that there is an attractive interaction with Ir and O atoms. However, the values of r_0 for both Ir-Ir and O-O pairs are larger than the nearest

neighbor distances, which makes these interactions repulsive. As a consequence, the MS-Q EFF developed is not suitable for investigating pure Ir or pure oxygen systems, since the bond distances cannot be captured correctly. The electronegativity (χ) and atomic hardness (J) values for Ir and O are different from those derived from ionization potentials and electron affinities for atoms,⁸¹ which are $\chi = 5.4$ eV and $J = 7.6$ eV for Ir, and $\chi = 7.54$ eV and $J = 12.16$ eV for O, respectively. The observed discrepancies are not surprising since the ionization potentials and electron affinities are different for a solid compared to an isolated atom.

Table 1. The fitted Morse potential parameters for Ir-O.

	Ir-Ir	Ir-O	O-O
D_e (eV)	0.008457	1.892584	0.026993
α (\AA^{-1})	1.537744	2.642281	1.614355
r_0 (\AA)	4.584917	1.8659	3.549025

Table 2. The fitted QEq parameters for Ir and O.

	Ir	O
χ (eV)	2.579346	10.189444
J (eV)	7.70769	13.231498
R (\AA)	1.261788	0.690854

Comparisons between the MS-Q estimated properties and corresponding DFT values are given in Figure 3 for binding energies (Figure 3a), elastic constants (Figure 3b), lattice parameters (Figure 3c) and internal coordinates (Figure 3d) of IrO₂ polymorphs. Figure 3a shows that the mean absolute error in the binding energies is 0.05 eV/IrO₂ and the correlation coefficient (R^2) is 0.972, which shows that the DFT energies are well reproduced in a wide range of energies for a wide variety of different structures. For the elastic constants in Figure 3b, a good correlation ($R^2 = 0.987$) is obtained between DFT and MS-Q and the mean absolute error is 18.4 GPa. A relatively large error in elastic constants is expected since these quantities are calculated from the second derivatives of the energy with respect to atomic positions, which are more sensitive to the parameter changes compared to other quantities. In Figure 3c and d, both lattice constants and internal coordinates obtained from MS-Q are very well correlated to the DFT values. For

both the observables, a near-perfect correlation ($R^2 = 0.999$) is obtained along with a low mean absolute error (0.1 Å and 0.007 respectively). Overall, the correlations in Figure 3 show that MS-Q accurately predicts the observed quantities calculated with DFT.

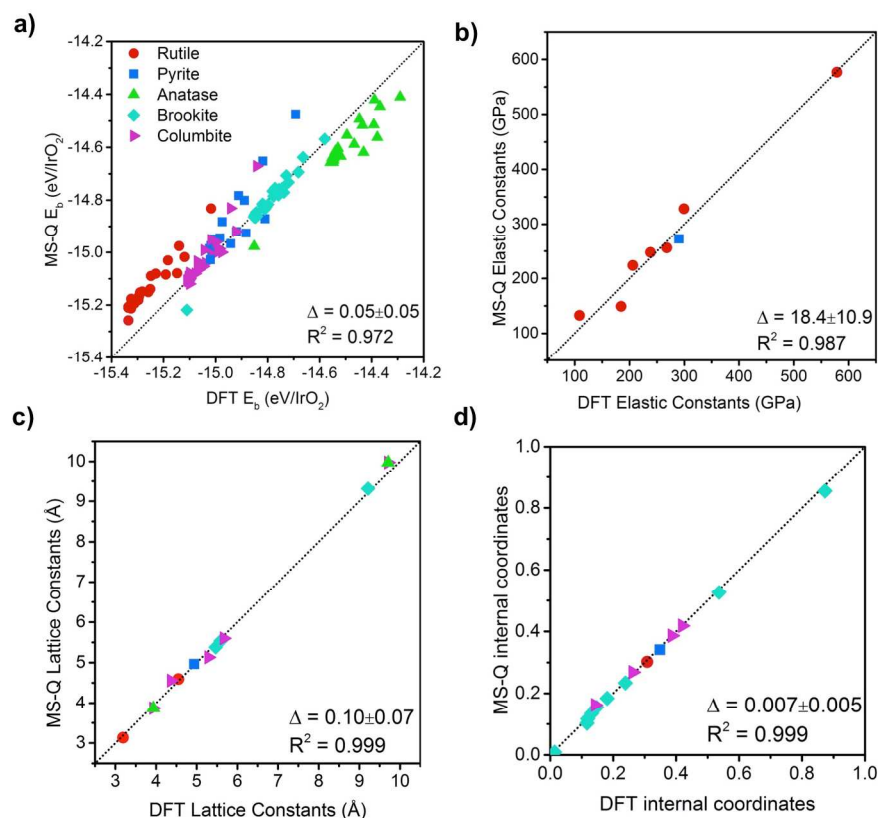


Figure 3. Goodness of fit comparisons between MS-Q and DFT for a) binding energies (E_b), b) elastic constants, c) lattice constants, and d) internal coordinates for the polymorphs of IrO_2 . The mean absolute error (Δ) with standard deviation and Pearson correlation coefficient (R^2) for each data set is given in corresponding plots.

3.2 Bulk properties

The lattice constants, internal coordinates, elastic constants and binding energy of the most stable rutile phase of IrO_2 obtained from MS-Q are listed in Table 3. The MS-Q force field predicts the lattice parameters of the rutile phase of IrO_2 as $a = 4.59$ Å and $c = 3.14$ Å, which are within 2% of the respective DFT values of 4.55 Å and 3.19 Å, and experimental values⁷¹ of 4.505 Å and 3.159 Å. The discrepancies in predicted elastic constants with MS-Q given in Table 3 are less than 20% of the DFT values, and the bulk modulus is predicted to within 5%. The phonon dispersion curves of the rutile IrO_2 along high

symmetry directions are also computed with MS-Q and shown in the Supporting Information. The phonon modes around the Γ -point compared well with DFT results.

Table 3. The lattice parameters (a and c), internal coordinate (x), elastic constants (C_{ij} 's and B) and binding energy (E_b) of the rutile phase of IrO_2 predicted using the MS-Q force field compared to the calculated DFT values, and available experimental data (Exp).

	DFT	Exp.	MS-Q
a (Å)	4.55	4.51	4.59
c (Å)	3.19	3.16	3.14
x	0.3081		0.3022
C_{11} (GPa)	294.6		328.3
C_{12} (GPa)	233.1		247.7
C_{13} (GPa)	183.3		149.0
C_{33} (GPa)	577.0		576.8
C_{44} (GPa)	106.4		132.7
C_{66} (GPa)	200.4		223.9
B (GPa)	268		256
E_b (eV/ IrO_2)	-15.33		-15.26

Table 4 compares the MS-Q calculated lattice parameters, internal coordinates and binding energies for IrO_2 polymorphs to the DFT values. For the high pressure pyrite phase, the value of $a = 4.96$ Å predicted from MS-Q is only 0.4% away from the DFT value and 1.8% higher than the experimental⁷² value of $a = 4.87$ Å. The bulk modulus of the pyrite phase ($B = 272$ GPa) also reasonably matches the DFT value of 290 GPa and is in good agreement with the experimental value of 306 GPa.⁷² Table 4 also shows that the structural parameters of the anatase, brookite and columbite phases obtained with MS-Q are good agreement with DFT. Most importantly, the relative stabilities of IrO_2 polymorphs follow $E_{coh}^{\text{Rutile}} < E_{coh}^{\text{Columbite}} < E_{coh}^{\text{Pyrite}} < E_{coh}^{\text{Brookite}} < E_{coh}^{\text{Anatase}}$, which is the stability order obtained from DFT calculations. Here, we find that the columbite phase is more stable than the pyrite phase at 0 K and 0 GPa, although the columbite phase has not been observed in experiments.⁷² Similar phase stability order for IrO_2 was also previously reported using PBE calculations, while PBEsol and AM05 functionals resulted in the pyrite phase being more stable than the columbite phase.³⁶

Table 4. Calculated lattice parameters (a , b , c), internal coordinates for O and Ir (x_{O} , x_{Ir} , y_{O} , y_{Ir} , z_{O} , z_{Ir}) and binding energies (E_b) of IrO₂ polymorphs compared to DFT.

Polymorph	DFT	MS-Q
Pyrite	$a = 4.94 \text{ \AA}$	$a = 4.96 \text{ \AA}$
	$x = 0.3486$	$x = 0.3413$
	$E_b = -15.02 \text{ eV}$	$E_b = -15.10 \text{ eV}$
	$B = 290 \text{ GPa}$	$B = 272 \text{ GPa}$
Anatase	$a = 3.93 \text{ \AA}$	$a = 3.87 \text{ \AA}$
	$c = 9.71 \text{ \AA}$	$c = 9.98 \text{ \AA}$
	$x = 0.2117$	$x = 0.2111$
	$E_b = -14.56 \text{ eV}$	$E_b = -14.69 \text{ eV}$
Columbite	$a = 4.37 \text{ \AA}$	$a = 4.56 \text{ \AA}$
	$b = 5.67 \text{ \AA}$	$b = 5.60 \text{ \AA}$
	$c = 5.29 \text{ \AA}$	$c = 5.13 \text{ \AA}$
	$y_{\text{Ir}} = 0.1425$	$y_{\text{Ir}} = 0.1619$
	$x_{\text{O}} = 0.2626$	$x_{\text{O}} = 0.2686$
	$y_{\text{O}} = 0.3868$	$y_{\text{O}} = 0.3862$
	$z_{\text{O}} = 0.4197$	$z_{\text{O}} = 0.4184$
	$E_b = -15.11 \text{ eV}$	$E_b = -15.22 \text{ eV}$
	$a = 9.21 \text{ \AA}$	$a = 9.31 \text{ \AA}$
	$b = 5.59 \text{ \AA}$	$b = 5.53 \text{ \AA}$
Brookite	$c = 5.46 \text{ \AA}$	$c = 5.38 \text{ \AA}$
	$x_{\text{Ir}} = 0.1313$	$x_{\text{Ir}} = 0.1340$
	$y_{\text{Ir}} = 0.1167$	$y_{\text{Ir}} = 0.1029$
	$z_{\text{Ir}} = 0.8729$	$z_{\text{Ir}} = 0.8458$
	$x_{\text{O}1} = 0.0141$	$x_{\text{O}1} = 0.0091$
	$y_{\text{O}1} = 0.1473$	$y_{\text{O}1} = 0.1548$
	$z_{\text{O}1} = 0.1810$	$z_{\text{O}1} = 0.1841$
	$x_{\text{O}2} = 0.2390$	$x_{\text{O}2} = 0.2336$
	$y_{\text{O}2} = 0.1192$	$y_{\text{O}2} = 0.1162$
	$z_{\text{O}2} = 0.5362$	$z_{\text{O}2} = 0.5267$
$E_b = -14.85 \text{ eV}$	$E_b = -15.03 \text{ eV}$	

Table 5. Comparison of average charge of Ir and O atoms in different polymorphs calculated with MS-Q with Bader charges calculated using DFT.

Polymorph	MS-Q		DFT - Bader	
	Ir	O	Ir	O
Rutile	+1.685	-0.843	+1.658	-0.829
Pyrite	+1.712	-0.856	+1.594	-0.797
Anatase	+1.644	-0.822	+1.632	-0.816
Columbite	+1.690	-0.845	+1.616	-0.808
Brookite	+1.672	-0.836	+1.619	-0.809

Apart from energetic, mechanical, and structural properties, it is also important to investigate whether the variable charge approach captures the electrostatic interactions in the system. We compare the atomic charges on Ir and O calculated with MS-Q to Bader charges⁸⁰ calculated using DFT for different IrO₂

polymorphs in Table 5. It is remarkable that despite the atomic charges not being explicitly included in the training set, we obtain excellent agreement between MS-Q and DFT Bader charges. For the rutile phase, the respective Ir and O charges of +1.685, and -0.843 match very well with the DFT Bader charges of +1.658 and -0.829, respectively. For other polymorphs, the MS-Q and Bader charges also match well with little discrepancy in the magnitude of charges relative to rutile phase.

3.3 Pressure-induced phase transitions

In order to validate the capability of the derived MS-Q force field in predicting bulk phase transitions, the pressure dependence of the enthalpy of IrO_2 polymorphs is evaluated between -10 and 30 GPa and compared to DFT predictions. DFT calculations in Figure 4(a) indicate a phase transition of IrO_2 from rutile to pyrite structure at a pressure ~ 18 GPa, while MS-Q predicts the same phase transition at pressure ~ 16 GPa. Although the columbite phase is found to be more stable than the pyrite phase at zero pressure, at high pressures the columbite phase becomes less stable and this phase is not expected to form at high pressures. The rutile-pyrite phase transition pressure obtained with MS-Q agrees very well with the current DFT results, and is also in agreement with previous experimental findings that report the existence of the pyrite phase above 15 GPa.⁷² The crossover between pyrite and columbite phases, which is present in the DFT data (Figure 4a), is not present in the MS-Q data. The discrepancy may be due to the inclusion of elastic constants only in the observed (pyrite, rutile), but not in the hypothetical (columbite, anatase, brookite), phases in the training set.

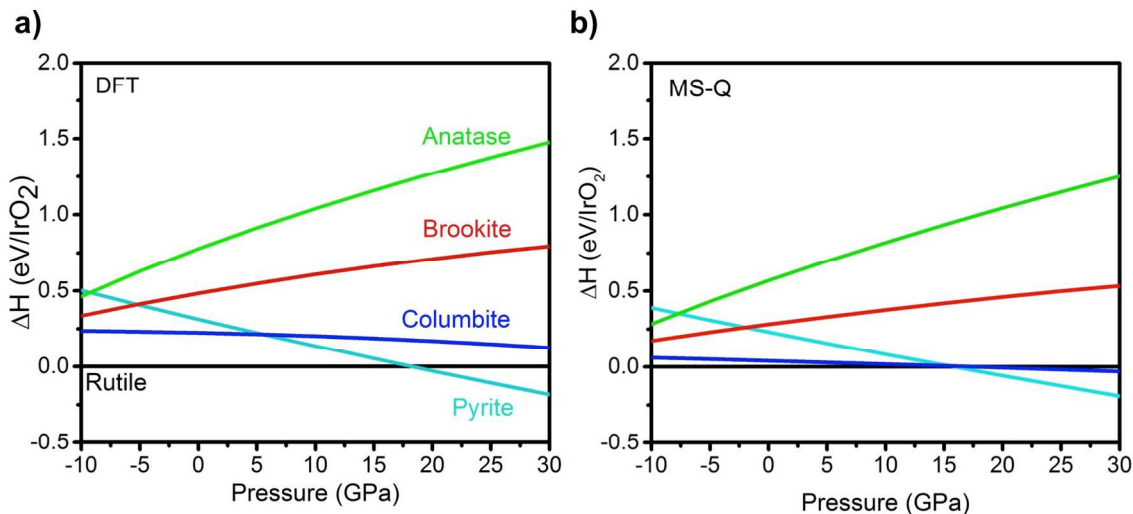


Figure 4. Enthalpy (ΔH) vs. pressure of IrO_2 polymorphs relative to the rutile phase calculated with a) DFT and b) MS-Q. The phase transition from rutile to pyrite occurred at 18 GPa with DFT and 16 GPa with MS-Q.

3.4 Vacancy formation energies

To predict nanoscale properties for catalysis applications, accurate prediction of surface properties and defect and adsorbate energetics is essential. Therefore, the formation energies of an oxygen vacancy (V_{O}), iridium vacancy (V_{Ir}), stoichiometric Ir+2O vacancy complex, for which Ir and O atoms are nearest neighbors ($V_{\text{Ir+2O-near}}$), and stoichiometric Ir+2O vacancy complex, for which Ir and O atoms are separated from each other by $> 5 \text{ \AA}$ ($V_{\text{Ir+2O-far}}$), are calculated with the fitted MS-Q force field and compared with corresponding DFT results. Table 6 summarizes the results. The vacancy formation energy ($E(V)$) was estimated using a $2 \times 2 \times 3$ supercell of the rutile phase (containing 24 formula units) using

$$E(V_{n\text{Ir}+m\text{O}}) = E_{\text{defect}} - E_{\text{perfect}} + nE(\text{Ir}) + mE(\text{O}) \quad (5)$$

where E_{defect} is the total energy of the defective system, E_{perfect} is the total energy of the supercell without defects, and n and m are the total number of Ir and O atoms missing in the defective structure, respectively. We have chosen to use the energies of the isolated atoms $E(\text{O})$ and $E(\text{Ir})$ as references to avoid confounding inaccuracies due to the O_2 energy and for ease of comparison with EFF results, in which the values of $E(\text{Ir})$ and $E(\text{O})$ are zero. Note in addition that only neutral vacancies are investigated.

Table 6. Vacancy formation energies (in eV) of the rutile IrO_2 phase calculated with the MS-Q force field, compared with those from DFT calculations. The formation energy of an oxygen vacancy (V_{O}), iridium vacancy (V_{Ir}), stoichiometric Ir+2O vacancies for which Ir and O atoms were nearest neighbors

($V_{\text{Ir}+2\text{O-near}}$) and stoichiometric Ir+2O vacancy for which Ir and O atoms are separated from each other by over 5 Å ($V_{\text{Ir}+2\text{O-far}}$). The energies for isolated atoms are used as references.

Defect	MS-Q	DFT
V_{O}	6.0	6.7
V_{Ir}	11.9	9.3
$V_{\text{Ir}+2\text{O-near}}$	20.5	20.8
$V_{\text{Ir}+2\text{O-far}}$	23.8	22.9

Table 6 shows that vacancy formation energies predicted from MS-Q correlates well ($R^2 = 0.9658$) with the corresponding DFT values, although vacancy formation energies are not part of the training set. The oxygen and stoichiometric vacancies are predicted to within 12% and 4%, respectively. The poorest accuracy is found in the formation energy of V_{Ir} , which is attributed to the weak O-O interactions defined in the Morse potential. When an Ir atom is removed from its octahedral site, the V_{Ir} is situated in between 6 O atoms that are separated by either 2.47 Å or 2.82 Å. This separation distance is smaller than the equilibrium distance of 3.55 Å in the Morse potential (Table 1) for the O-O pair, so that around the V_{Ir} , the attractive interactions between O atoms could not be represented.

The formation energy of the stoichiometric vacancy complex $V_{\text{Ir}+2\text{O}}$ calculated with MS-Q is found to be very similar to the DFT value when the vacancies are nearest neighbors. When the vacancies are separated, the discrepancy in formation energies between DFT and MS-Q is increased. For the far separated (5 Å) $V_{\text{Ir}+2\text{O}}$ defect complex, the binding energy, *i.e.* $E(V_{\text{Ir}+2\text{O}}) - E(V_{\text{Ir}}) - 2E(V_{\text{O}})$, are only 0.06 eV and 0.17 eV for MS-Q and DFT, respectively. Consequently, the interactions among vacancy defects are already quite weak at this distance. The increase in the error for defect formation energies of far separated $V_{\text{Ir}+2V_{\text{O}}}$ complex is likely due to the error in V_{Ir} and weak O-O interaction. Overall, the vacancy formation energies are reasonably well represented with the fitted MS-Q force field.

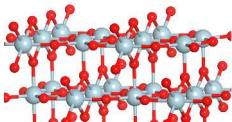
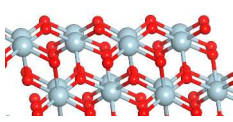
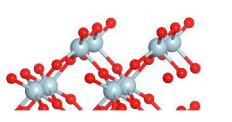
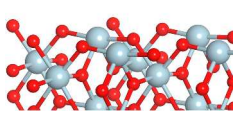
3.5 Surface properties

To test the derived MS-Q potential on surface properties of IrO_2 , the energies (γ) of low index surfaces of rutile IrO_2 namely, (110), (101), (100) and (001), are computed with the MS-Q potential and compared to our DFT results and earlier revPBE³⁸ calculations in Table 7. Recall that surface energies for (110) and (100) are part of the training set, whereas the others are not. Table 7 shows strong agreement between the γ values obtained with MS-Q and with DFT for all of the surfaces considered. In both MS-Q

and DFT, the (110) surface is the most stable, and the relative stability of surfaces follows the order $\gamma^{(110)} < \gamma^{(101)} < \gamma^{(100)} < \gamma^{(001)}$, which matches well with the results for other rutile structures.⁸² The maximum difference in γ values between DFT and MS-Q was 0.2 J/m². The similarity of γ values obtained with MS-Q and DFT is also evident in the constructed Wulff shape⁸³ shown in Figure 5. Wulff shape of rutile IrO₂ created using a) DFT and b) MS-Q computed low index surface energies, showing the predicted crystal shape. Both DFT (Figure 5a) and MS-Q (Figure 5b) predict a similar surface structure and crystallite shape for rutile IrO₂, but MS-Q predicts a slightly larger area coverage for the (100) facets compared to DFT.

In a previous⁵¹ MS-Q force field developed for Ti-O system, the relative energies for different TiO₂ surfaces were incorrect, which was explained by the low charges imposed on atoms in their model. However in that model for Ti-O, the QEq parameters were not optimized for the system. In this study, we find that inclusion of energies of (110) and (100) surfaces in the training set and optimization of the QEq parameters is instrumental in obtaining realistic charges on Ir and O atoms (see Table 5), and very accurate surface energies compared to DFT results (Table 7). In the determination of the charge q for each ion using QEq, electronegativity (χ) difference between dissimilar atoms determines the amount of charge transfer, whereas the hardness (J) determines how easily an element can donate/accept charges. Rappe and Goddard's QEq parameters⁴³ result in $q_{\text{Ir}} \sim +0.8$ and $q_{\text{O}} \sim -0.4$, which are far from realistic. We attempted fitting with constraining the charges to published results, but could not find a parameter set that can give both surface and bulk properties correctly.

Table 7. Surface energies, γ , for several low index surfaces of IrO₂. The surface atomic structure is depicted for each surface at the top.

	 γ (110) (J/m ²)	 γ (101) (J/m ²)	 γ (100) (J/m ²)	 γ (001) (J/m ²)
MS-Q	1.58	1.69	1.88	2.18
PBE+U+SOC	1.38	1.62	1.85	2.31
revPBE	1.05	1.24	1.35	1.94

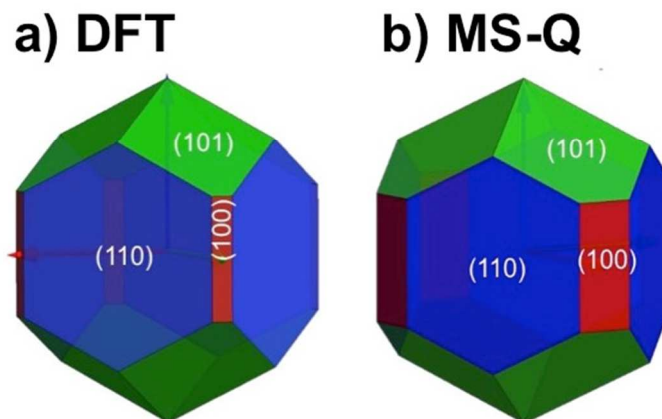


Figure 5. Wulff shape of rutile IrO_2 created using a) DFT and b) MS-Q computed low index surface energies, showing the predicted crystal shape.

3.6 O adsorption on rutile (110) surface and IrO_2 nanocrystal

For the study of catalytic processes involved in the OER and water splitting, oxygen adsorption energies are found to be a good descriptor for catalytic activity, because of its linear correlation with HO and HOO binding on oxide surfaces.³⁴ We therefore test the accuracy of the MS-Q EFF in predicting oxygen adsorption energies. The adsorption energy (E_{ad}) of a single O atom on rutile IrO_2 (110) 2×1 surface was calculated at three different sites, namely Ir-top, bridge and O-top as shown in Figure 6. The value of E_{ad} calculated with MS-Q and DFT are defined by

$$E_{ad} = E_{slab+O} - E_{slab} - E(O) \quad (6)$$

where E_{slab+O} is the total energy of the (110) surface slab with the adsorbed O atom and E_{slab} is the total energy of the pristine (110) surface slab. Again we use the isolated O atom for the reference energy $E(O)$. In DFT, $E(O)$ is calculated in a $20 \text{ \AA} \times 20 \text{ \AA} \times 20 \text{ \AA}$ box, whereas in MS-Q, $E(O)$ is zero. E_{ad} values calculated using MS-Q, and comparisons to DFT results are listed in Table 8. MS-Q correctly predicts the relative order in the E_{ad} with respect to different surface sites when compared to DFT. Among the three sites, the Ir-top site is found to be the most favorable site for O adsorption, the bridge site has an intermediate E_{ad} , and the O-top site is the least favorable adsorption site. The predicted values of E_{ad} with MS-Q for Ir-top and bridge sites are within 30% of DFT values. The bond length of the adsorbed O and the surface atoms of rutile (110) are given in Figure 6. The Ir-O bond lengths between the surface Ir and

adsorbed O atoms calculated with MS-Q are in very good agreement with DFT calculations. As expected, there is considerable discrepancy between MS-Q and DFT calculated E_{ad} values for the O-top site. The weak interaction and a large r_0 value of 3.55 Å defined in the Morse potential for the O-O pair (see Table 1) results in a large MS-Q predicted bond length of adsorbed O to surface. MS-Q predicts O-O bond length of 3.07 Å compared to 1.32 Å obtained with DFT. As a consequence, the E_{ad} was not predicted accurately for the O-top site. We conclude that as long as highly unfavorable sites – which are not relevant to the catalytic processes anyway – are avoided, MS-Q is well suited to study adsorption energetics on IrO₂ surfaces.

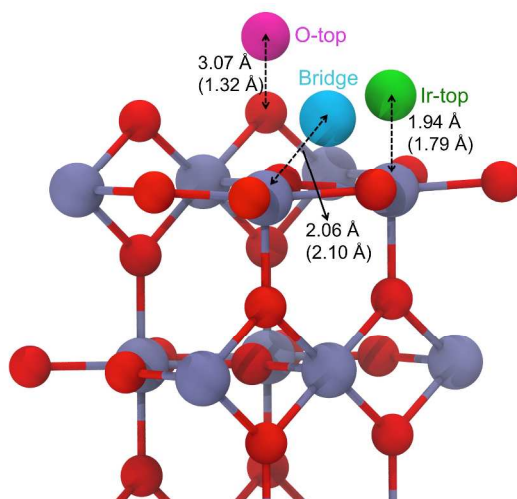


Figure 6. Atomic O adsorption on rutile (110) surface. The bond length of the adsorbed O and its nearest surface atom at O-top, Ir-top, and bridge sites are indicated on each adsorption site. Similar calculations carried out with DFT and corresponding values are given in parentheses.

Table 8. Adsorption energies (E_{ad}) of atomic oxygen at different sites on rutile IrO₂ (110) surface.

Adsorption site	MS-Q (eV/O atom)	DFT (eV/O atom)
Ir-top	-3.17	-4.34
Bridge	-1.98	-2.80
O-top	-0.83	-2.43

In Figure 5, it was shown that IrO₂ crystals have a faceted structure composed of (110), (101) and (100) surfaces and the O adsorption characteristics can be different at the edges and corners of the crystal. To investigate the O adsorption energetics on an IrO₂ crystal, we constructed a nanocrystal of IrO₂ with a diameter of ~2.5 nm based on the Wulff construction. The dimensions of the nanocrystal are given in

Figure 7a and b. The constructed nanocrystal has 785 atoms, i.e. 261 Ir and 524 O atoms. The nanostructure is nearly stoichiometric with an O:Ir ratio of 2.008. It should be noted that DFT calculations of a nanocrystal of this size are computationally very expensive.

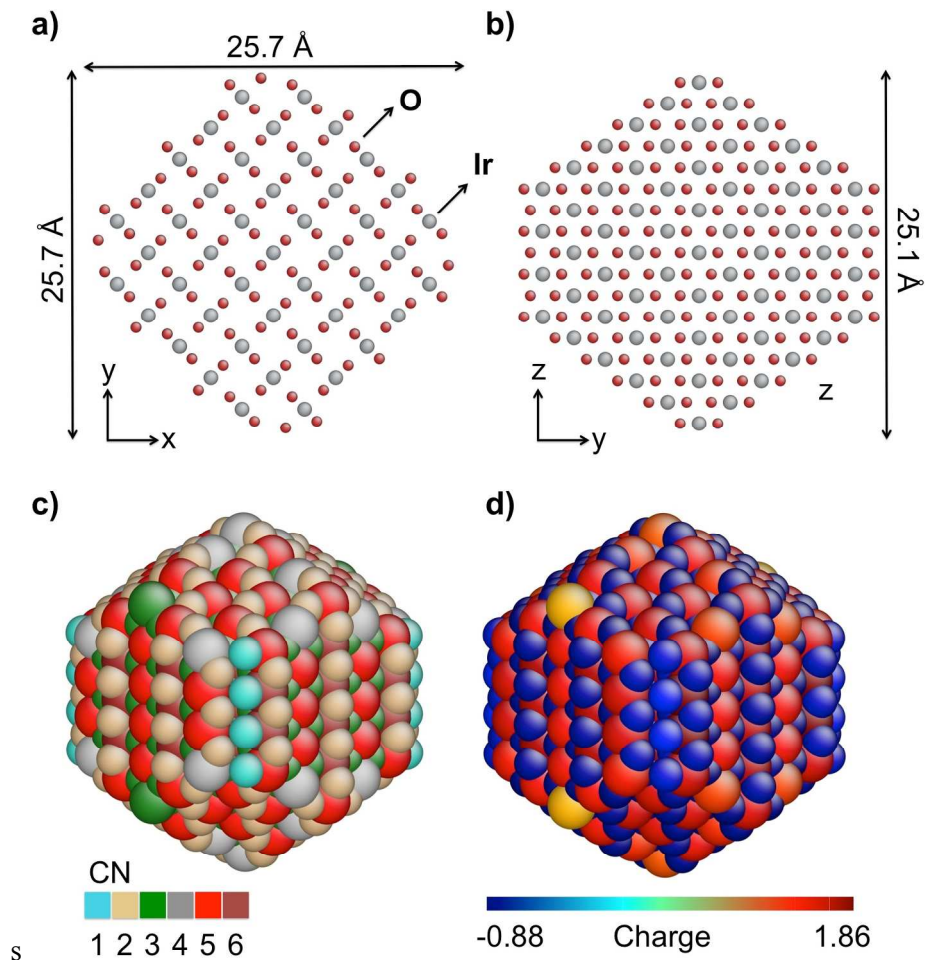


Figure 7. Atomic structure of an IrO_2 nanocluster built using the Wulff construction. The dimensions of the nanoclusters are given in a) xy-projection and b) yz projection. The atoms are colored according to their coordination number (CN) in c) and atomic charges in d).

The activity of a catalyst has been reported^{32, 33} to be strongly correlated with the geometry of the surface. In particular, a change in the coordination number (CN) of atoms at steps, kinks, and terraces plays a major role in catalytic performance. The CNs on facets, edges and corners of a nanocrystal are different from those in the bulk or surfaces, which should offer sites of varying catalytic properties. Figure 7c shows the CN of atoms in the nanocrystal (rendered with the AtomEye⁸⁴ software) and indicates that Ir and O atoms at the facets, edges and corners formed at the intersection of the facets have

lower coordination compared to Ir and O in bulk and on planar surfaces. It should be noted that in rutile IrO_2 , Ir and O has CN of 6 and 3, respectively. The CN of surface Ir atoms are particularly important to the O adsorption properties, since surface Ir atoms are the most preferable adsorption site for O as shown in Table 8. The lowest CN for Ir of 3 is found at the corner formed between the facets of $(\bar{1}0\bar{1})$, $(0\bar{1}1)$ and $(1\bar{1}0)$. Ir atoms at the edges of $\{110\}$ and $\{101\}$ facets and corners also have a low CN of 4.

For an oxide catalyst, electrostatic interactions may play a role in determining the catalytic activities of different sites. To investigate the effect of electrostatics, we study the charges determined for each atom under the QEq scheme. The calculated atomic charges at the surface of nanoclusters are shown in Figure 7d. In correlation with the CN, Ir atoms at the surface have lower atomic charges compared to bulk Ir with $q_{\text{Ir}} = 1.69$. The lowest charge, $q_{\text{Ir}} = 1.03$, is found at the corner of $(\bar{1}0\bar{1})$, $(0\bar{1}1)$ and $(1\bar{1}0)$ facets, corresponding to the lowest CN.

To investigate the effects of CN and electrostatics on catalytic activities, we calculate the O adsorption energy on selected sites on the IrO_2 nanocrystal, chosen to have varying CN and atomic charges, as shown in Figure 8. We expect the O adsorption energy (E_{ad}), which is used as a descriptor for the catalytic activity in water splitting and oxygen evolution reactions, to vary with location on the nanocrystal. We consider surface Ir top sites on (110) and (101) surfaces, edges and corners formed at the intersection of $\{110\}$, $\{100\}$ and $\{101\}$ facets.

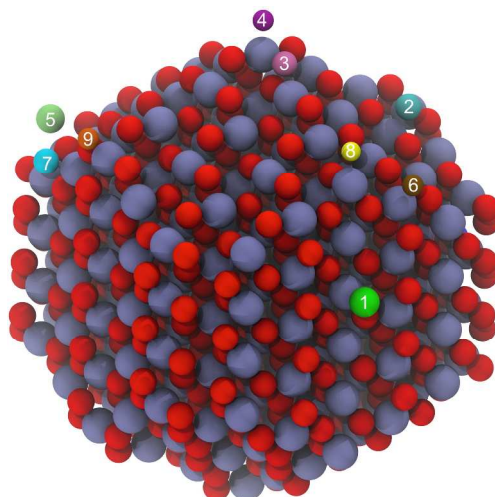


Figure 8. Adsorption sites considered on IrO₂ nanocluster. Large atoms are Ir and small atoms are O. The adsorbed oxygen atoms at the corresponding site were numbered and colored differently.

Table 9. Oxygen adsorption energies (E_{ad}) at different sites on the IrO₂ nanocrystal. The coordination number (CN) of the surface Ir atom that O binded and the length of the bond formed between Ir and adsorbed O (d_{Ir-O}) is given.

#	Adsorption site	Ir CN	E_{ad} (eV/O atom)	d_{Ir-O} (Å)
1	(110) Ir top	5	-3.22	1.98
2	(101) Ir top	5	-3.06	1.95
3	(101) (101) edge bridge	4	-4.08	2.01
4	(101) (101) corner	4	-3.37	1.92
5	(110) (100) edge	4	-3.14	1.93
6	(110) (101) edge 1	5	-3.05	1.97
7	(110) (101) edge 2	4	-3.44	1.92
8	(110) (101) (101) corner 1	3	-4.54	1.87
9	(110) (101) (101) corner 2	5	-2.71	1.95

E_{ad} values calculated at these different surface sites are summarized in Table 9. Figure 8 and Table 9 indicate that corner sites at the IrO₂ nanocrystal surface have up to 1.4 eV/O lower binding energy for O compared to bare (110) and (101) surfaces. Site #1 is the same as the Ir-top site on the (110) surface slab in Figure 8, and has a similar E_{ad} of -3.22 eV/atom on the nanocrystal compared to -3.17 eV/atom on the surface slab. This similarity confirms that the (110) surface on the nanocrystal is large enough to mimic the O adsorption on periodic surface slab calculations and no significant effects of edge and corner sites exist for O adsorption calculations. In Table 9, the lowest E_{ad} is calculated to be -4.54 eV/atom for site #8 in Figure 8, which is the corner formed at the intersection of {110}, {100} and {101} facets. This Ir site

also had the lowest CN of 3 (Figure 7c). The second most favorable site with E_{ad} of -4.08 eV/atom is #3 in Figure 8, which is an Ir bridge site formed at the edge of the $\{101\}$ facets, with CN of 4. The other edge sites considered have similar E_{ad} values compared to E_{ad} on the (110) surface (#1 in Table 9).

It is interesting to note that there is a wide variation in the E_{ad} values for similarly coordinated adsorption sites as shown in Figure 9a. Although E_{ad} values are strongly correlated with the CN of surface Ir atom, the local CN alone cannot explain the differences in the adsorption energies between the various sites. We explored the correlation of the long-range electrostatic interactions and the adsorption energies by evaluating E_{ad} with respect to the atomic charge transfer between the surface Ir atom and the adsorbed O (O^*). In the QEq method, due to charge neutrality in the system, the atomic charge on the O^* can be used to quantify the charge transfer in the system with the O adsorption. We observe a stronger correlation between the q_{O^*} and the E_{ad} values ($R^2 \sim 0.73$), when compared to the correlation between CN and E_{ad} ($R^2 \sim 0.67$). Remarkably, if we consider sites with the same CN separately, the correlation between CN and E_{ad} becomes almost perfectly linear, as shown in Figure 9b. For both CN of 4 and 5, E_{ad} becomes more negative with the increase in the absolute q_{O^*} values ($R^2 \sim 0.98$ and 0.99 respectively). Comparison of Figure 9 (a) vs. (b) thus suggests that OER activity at under-coordinated sites is strongly influenced by long-range electrostatics around the geometrical features on IrO_2 nanocrystal surfaces, rather than only on local coordination as previously reported for transition metals.^{32, 33} These results indicate that the local coordination-dependent catalytic activity of metal oxides can be different than transition metals such that charge transfer at the surfaces influenced by the long-range electrostatics also has a significant contribution to the catalytic activity in addition to coordination number of active surface sites. Indeed, spectroscopic observations on metal oxide catalyst surfaces for water splitting reaction reported⁸⁵ formation of intermediate oxidation states for the Ir atoms at the surface of IrO_x nanoclusters,^{86, 87} which can be attributed to the charge transfer processes between the adsorbate and the metal at the metal-oxide nanocrystal surfaces, although no direct measurements of charge transfer processes could be attained due to experimental limitations of complicated chemistry at nanoscale. Using the MS-Q EFF we

developed, we are able to reveal the charge transfer dependent catalytic activity on IrO₂ nanoclusters. These results also signify that the inclusion of variable charge treatment in MS-Q is essential for capturing the observed variations in adsorption energies. With this knowledge, one can engineer the catalytic activity of IrO₂ nanocrystals by selectively creating surface features to maximize the catalytic performance. The MS-Q force field can be further used to investigate size and shape effects on binding properties of IrO₂ nanoclusters.

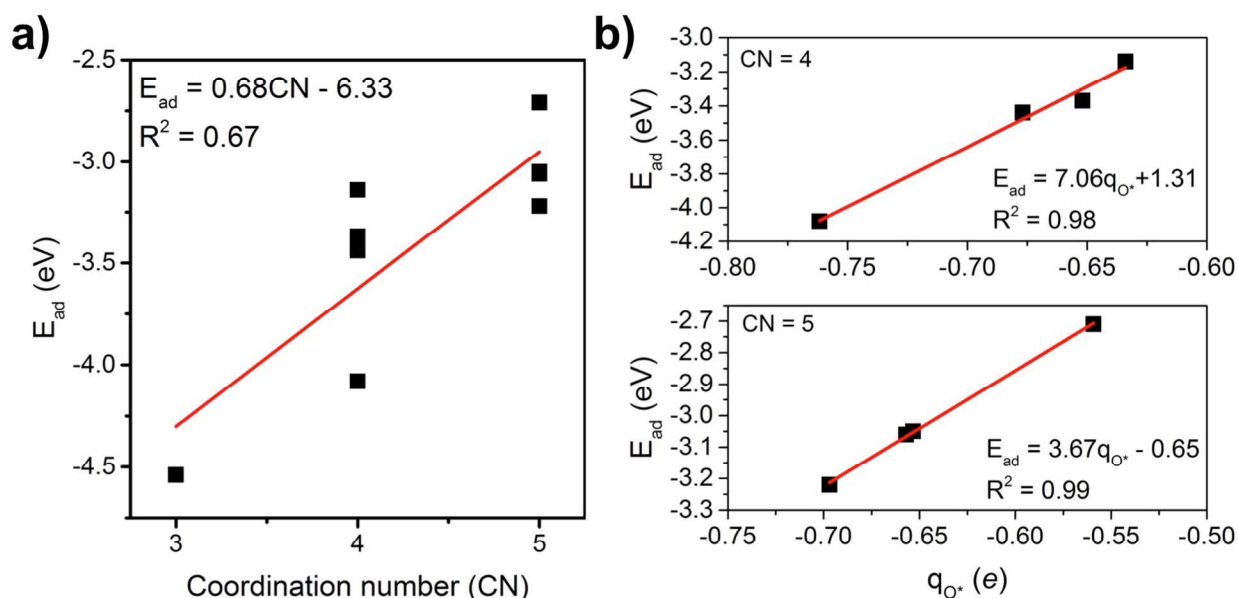


Figure 9. Change in the adsorption energy (E_{ad}) of a single O atom with respect to the a) coordination number (CN), b) charge of adsorbed O atom (q_{O^*}) for Ir CN of 4 and 5. The line at each plot is obtained from least squares fitting to a linear equation, and corresponding best-fit equations and R^2 values are given at the insets in each figure.

4. Conclusions

A first principles-based force-field for the Ir-O system was developed by parameterizing a Morse potential coupled with a variable charge equilibration method (QEq) (MS-Q). The MS-Q parameters were fit to the DFT-derived bulk, surface, structural and thermodynamic properties of IrO₂ polymorphs using a genetic algorithm. The use of a variable charge model and genetic algorithm in the fitting enabled very accurate description of electrostatic interactions such that the bulk properties such as binding energies, elastic constants, lattice constants and internal coordinates as well as surface and defect properties compared very well with the DFT results. The critical pressure predicted with MS-Q for rutile to pyrite

phase transformations agreed well with DFT predictions. MS-Q predicted with reasonable accuracy the vacancy formation energies. The surface energies and O binding on Ir sites on IrO₂ surfaces were also represented very well with the MS-Q force field. Overall, we find that both bulk and surface properties were predicted reasonably well with MS-Q force field compared to DFT. Based on the adsorption and binding energetics, it can be inferred that catalytic properties of IrO₂ nanoclusters pertaining to oxygen evolution, and water splitting reactions are drastically enhanced at the edges and corners on the IrO₂ nanocrystals. The improved OER activity at under-coordinated sites appears to have a strong dependence on long-range electrostatics rather than only on local coordination. Successful prediction of the above properties by MS-Q represents an important step towards understanding size-dependent structural stability and activity of nanocatalysts and will aid in rational design of nanocatalysts. The force field developed in this work should enable large-scale atomistic modeling of Ir-O systems and therefore be useful for gaining atomistic insights into structure, catalytic, and dynamic properties of IrO₂ nanoclusters, nanoparticles, and phases of relevance to a range of energy applications.

Acknowledgements

We acknowledge C. Wolverton and J. Greeley for helpful discussions regarding the use of genetic algorithm for force field fitting. Use of the Center for Nanoscale Materials was supported by the U. S. Department of Energy, Office of Science, Office of Basic Energy Sciences, under Contract No. DE-AC02-06CH11357. We gratefully acknowledge the computing resources provided on Blues and Fusion, high-performance computing clusters operated by the Laboratory Computing Resource Center at Argonne National Laboratory. This work used the Extreme Science and Engineering Discovery Environment (XSEDE), which is supported by National Science Foundation grant number ACI-1053575.⁸⁸

Supporting Information Available: Vibration properties of rutile IrO₂ predicted by MS-Q and DFT (PDF). This material is available free of charge via the Internet at <http://pubs.acs.org>.

References

1. T. Nakamura, Y. Nakao, A. Kamisawa and H. Takasu, *Appl. Phys. Lett.*, 1994, **65**, 1522-1524.

2. C. S. Hwang, B. T. Lee, C. S. Kang, J. W. Kim, K. H. Lee, H. J. Cho, H. Horii, W. D. Kim, S. I. Lee, Y. B. Roh and M. Y. Lee, *J. Appl. Phys.*, 1998, **83**, 3703-3713.
3. C. Comninellis and G. P. Vercesi, *J. Appl. Electrochem.*, 1991, **21**, 335-345.
4. D. C. Kim, M. J. Lee, S. E. Ahn, S. Seo, J. C. Park, I. K. Yoo, I. G. Baek, H. J. Kim, E. K. Yim, J. E. Lee, S. O. Park, H. S. Kim, U. I. Chung, J. T. Moon and B. I. Ryu, *Appl. Phys. Lett.*, 2006, **88**, 232106.
5. K. Fujiwara, Y. Fukuma, J. Matsuno, H. Idzuchi, Y. Niimi, Y. Otani and H. Takagi, *Nat. Comm.*, 2013, **4**, 2893.
6. Y. Hirata, K. Ohgushi, J.-i. Yamaura, H. Ohsumi, S. Takeshita, M. Takata and T.-h. Arima, *Phys. Rev. B*, 2013, **87**, 161111R.
7. S. K. Panda, S. Bhowal, A. Delin, O. Eriksson and I. Dasgupta, *Phys. Rev. B*, 2014, **89**, 155102.
8. G. Wang, M. Zhou, J. T. Goettel, G. J. Schrobilgen, J. Su, J. Li, T. Schloeder and S. Riedel, *Nature*, 2014, **514**, 475-477.
9. A. Fog and R. P. Buck, *Sensor. Actuator.*, 1984, **5**, 137-146.
10. S. Yao, M. Wang and M. Madou, *J. Electrochem. Soc.*, 2001, **148**, H29-H36.
11. K. Izutsu and H. Yamamoto, *Anal. Sci.*, 1996, **12**, 905-909.
12. G. Beni, L. M. Schiavone, J. L. Shay, W. C. Dautremontsmith and B. S. Schneider, *Nature*, 1979, **282**, 281-283.
13. S. Song, H. Zhang, X. Ma, Z. Shao, R. T. Baker and B. Yi, *Int. J. Hydrogen Energ*, 2008, **33**, 4955-4961.
14. J. Suntivich, K. J. May, H. A. Gasteiger, J. B. Goodenough and Y. Shao-Horn, *Science*, 2011, **334**, 1383-1385.
15. Y. Lee, J. Suntivich, K. J. May, E. E. Perry and Y. Shao-Horn, *J. Phys. Chem. Lett.*, 2012, **3**, 399-404.
16. Y. Tachibana, L. Vayssieres and J. R. Durrant, *Nat. Photonics*, 2012, **6**, 511-518.
17. N. S. Lewis and D. G. Nocera, *Proc. Natl. Acad. Sci. U.S.A.*, 2006, **103**, 15729-15735.
18. H. B. Gray, *Nat. Chem.*, 2009, **1**, 7.
19. J. Marshall, *Nature*, 2014, **510**, 22-24.
20. A. Listorti, J. Durrant and J. Barber, *Nat. Mater.*, 2009, **8**, 929-930.
21. A. Fujishima and K. Honda, *Nature*, 1972, **238**, 37-38.
22. O. Khaselev and J. A. Turner, *Science*, 1998, **280**, 425-427.
23. X. Zhou, J. Yang and C. Li, *J. Phys. Chem. A*, 2012, **116**, 9985-9995.
24. J. C. Cruz, V. Baglio, S. Siracusano, R. Ornelas, L. Ortiz-Frade, L. G. Arriaga, V. Antonucci and A. S. Arico, *J. Nanopart. Res.*, 2011, **13**, 1639-1646.
25. S. D. Tilley, M. Cornuz, K. Sivula and M. Graetzel, *Angew. Chem. Int. Ed.*, 2010, **49**, 6405-6408.
26. J. D. Blakemore, M. W. Mara, M. N. Kushner-Lenhoff, N. D. Schley, S. J. Konezny, I. Rivalta, C. F. A. Negre, R. C. Snoeberger, O. Kokhan, J. Huang, A. Stickrath, L. A. Tran, M. L. Parr, L. X. Chen, D. M. Tiede, V. S. Batista, R. H. Crabtree and G. W. Brudvig, *Inorg. Chem.*, 2013, **52**, 1860-1871.
27. J. Huang, J. D. Blakemore, D. Fazi, O. Kokhan, N. D. Schley, R. H. Crabtree, G. W. Brudvig and D. M. Tiede, *Phys. Chem. Chem. Phys.*, 2014, **16**, 1814-1819.
28. R.-S. Chen, A. Korotcov, H. Ying-Sheng and T. Dah-Shyang, *Nanotechnology*, 2006, **17**, R67-R87.
29. M. T. M. Koper, *Nanoscale*, 2011, **3**, 2054-2073.
30. R. S. Chen, Y. S. Huang, Y. M. Liang, C. S. Hsieh, D. S. Tsai and K. K. Tiong, *Appl. Phys. Lett.*, 2004, **84**, 1552-1554.
31. K. A. Stoerzinger, L. Qiao, M. D. Biegalski and Y. Shao-Horn, *J. Phys. Chem. Lett.*, 2014, **5**, 1636-1641.
32. L. M. Falicov and G. A. Somorjai, *Proc. Natl. Acad. of Sci. U.S.A.*, 1985, **82**, 2207-2211.
33. F. Calle-Vallejo, D. Loffreda, M. T. M. Koper and P. Sautet, *Nat. Chem.*, 2015, **7**, 403-410.

34. J. Rossmeis, Z. W. Qu, H. Zhu, G. J. Kroes and J. K. Norskov, *J. Electroanal. Chem.*, 2007, **607**, 83-89.
35. J. S. de Almeida and R. Ahuja, *Phys. Rev. B*, 2006, **73**, 165102.
36. P. Mehta, P. A. Salvador and J. R. Kitchin, *ACS Appl. Mater. Interfaces*, 2014, **6**, 3630-3639.
37. S. Ono, J. P. Brodholt and G. D. Price, *J. Phys. Condens Mat.*, 2008, **20**, 045202.
38. G. Novell-Leruth, G. Carchini and N. Lopez, *J. Chem. Phys.*, 2013, **138**, 194706.
39. M. Matsui and M. Akaogi, *Mol. Simul.*, 1991, **6**, 239-244.
40. D. A. Case, T. E. Cheatham, T. Darden, H. Gohlke, R. Luo, K. M. Merz, A. Onufriev, C. Simmerling, B. Wang and R. J. Woods, *J. Comput. Chem.*, 2005, **26**, 1668-1688.
41. B. R. Brooks, C. L. Brooks, III, A. D. Mackerell, Jr., L. Nilsson, R. J. Petrella, B. Roux, Y. Won, G. Archontis, C. Bartels, S. Boresch, A. Caflisch, L. Caves, Q. Cui, A. R. Dinner, M. Feig, S. Fischer, J. Gao, M. Hodoscek, W. Im, K. Kuczera, T. Lazaridis, J. Ma, V. Ovchinnikov, E. Paci, R. W. Pastor, C. B. Post, J. Z. Pu, M. Schaefer, B. Tidore, R. M. Venable, H. L. Woodcock, X. Wu, W. Yang, D. M. York and M. Karplus, *J. Comput. Chem.*, 2009, **30**, 1545-1614.
42. W. J. Mortier, S. K. Ghosh and S. Shankar, *J. Am. Chem. Soc.*, 1986, **108**, 4315-4320.
43. A. K. Rappe and W. A. Goddard III, *J. Phys. Chem.*, 1991, **95**, 3358-3363.
44. D. M. York and W. T. Yang, *J. Chem. Phys.*, 1996, **104**, 159-172.
45. Y. Ma and S. H. Garofalini, *J. Chem. Phys.*, 2006, **124**, 084505.
46. R. A. Nistor, J. G. Polihronov, M. H. Muser and N. J. Mosey, *J. Chem. Phys.*, 2006, **125**, 094108.
47. E. Demiralp, T. Cagin and W. A. Goddard, *Phys. Rev. Lett.*, 1999, **82**, 1708-1711.
48. V. Swamy and J. D. Gale, *Phys. Rev. B*, 2000, **62**, 5406-5412.
49. Q. Zhang, T. Cagin, A. van Duin, W. A. Goddard, Y. Qi and L. G. Hector, *Physical Review B*, 2004, **69**, 045423.
50. A. Hallil, R. Tetot, F. Berthier, I. Braems and J. Creuze, *Phys. Rev. B*, 2006, **73**, 165406.
51. V. Swamy, J. Muscat, J. D. Gale and N. M. Harrison, *Surf. Sci.*, 2002, **504**, 115-124.
52. T. Back, U. Hammel and H. P. Schwefel, *IEEE Trans. Evol. Comput.*, 1997, **1**, 3-17.
53. E. Zitzler, M. Laumanns and S. Bleuler, in *Metaheuristics for multiobjective optimisation*, Springer, 2004, pp. 3-37.
54. U. Diwekar, *Introduction to Applied Optimization*, Springer Science & Business Media, LLC, 2008.
55. G. Kresse and J. Hafner, *Phys. Rev. B*, 1994, **49**, 14251-14269.
56. G. Kresse and J. Furthmuller, *Comp. Mater. Sci.*, 1996, **6**, 15-50.
57. J. P. Perdew, K. Burke and M. Ernzerhof, *Phys. Rev. Lett.*, 1996, **77**, 3865-3868.
58. G. Kresse and D. Joubert, *Phys. Rev. B*, 1999, **59**, 1758-1775.
59. P. E. Blochl, *Phys. Rev. B*, 1994, **50**, 17953-17979.
60. A. I. Liechtenstein, V. I. Anisimov and J. Zaanen, *Phys. Rev. B*, 1995, **52**, R5467-R5470.
61. S. L. Dudarev, G. A. Botton, S. Y. Savrasov, C. J. Humphreys and A. P. Sutton, *Phys. Rev. B*, 1998, **57**, 1505-1509.
62. H. Kleykamp and L. J. Paneth, *J. Inorg. Nucl. Chem.*, 1973, **35**, 477-482.
63. E. H. P. Cordfunke, *Thermochim. Acta*, 1981, **50**, 177-185.
64. C. Mallika, O. M. Sreedharan and M. S. Chandrasekharaiah, *J. Less-Common Met.*, 1985, **107**, 203-212.
65. O. Kubaschewski, C. B. Alcock and P. J. Spencer, *Materials Thermochemistry*, Pergamon Press, Oxford ; New York, 6th edn., 1993.
66. D. R. Lide, *CRC Handbook of Chemistry and Physics 87th ed.*, CRC Press, Boca Raton, FL, 2006.
67. S. Grindy, B. Meredig, S. Kirklin, J. E. Saal and C. Wolverton, *Phys. Rev. B*, 2013, **87**, 075150.
68. L. Wang, T. Maxisch and G. Ceder, *Phys. Rev. B*, 2006, **73**, 195107.
69. C. Kittel and P. McEuen, *Introduction to solid state physics*, Wiley New York, 1976.
70. R. R. Daniels, G. Margaritondo, C. A. Georg and F. Levy, *Phys. Rev. B*, 1984, **29**, 1813-1818.
71. A. A. Bolzan, C. Fong, B. J. Kennedy and C. J. Howard, *Acta Crystallogr. B*, 1997, **53**, 373-380.

72. S. Ono, T. Kikegawa and Y. Ohishi, *Physica B*, 2005, **363**, 140-145.
73. J. D. Gale and A. L. Rohl, *Mol. Simul.*, 2003, **29**, 291-341.
74. D. E. Goldberg, B. Korb and K. Deb, *Complex Systems*, 1989, **3**, 493-530.
75. K. Sastry and D. E. Goldberg, *Intelligent Engineering Systems Through Artificial Neural Networks*, 2001, **11**, 129-134.
76. K. Deb and A. Kumar, *Complex Systems*, 1995, **9**, 431-454.
77. K. Deb and R. B. Agrawal, *Complex Systems*, 1995, **9**, 115-148.
78. K. Sastry, *Single and multiobjective genetic algorithm toolbox in C++*, University of Illinois at Urbana-Champaign, Urbana, IL, 2007.
79. R. F. W. Bader, *Acc. Chem. Res.*, 1985, **18**, 9-15.
80. G. Henkelman, A. Arnaldsson and H. Jonsson, *Comp. Mater. Sci.*, 2006, **36**, 354-360.
81. R. G. Pearson, *Inorg. Chem.*, 1988, **27**, 734-740.
82. H. Perron, C. Domain, J. Roques, R. Drot, E. Simoni and H. Catalette, *Theor. Chem. Acc.*, 2007, **117**, 565-574.
83. R.V. Zucker, D. Chatain, U. Dahmen, S. Hagege and W.C. Carter, *J. Mater. Sci.* 2012, **47**, 8290-8302.
84. J. Li, *Model. Simul. Mater. Sci. Eng.*, 2003, **11**, 173-177.
85. M. Zhang and H. Frei, *Catal. Lett.*, 2015, **145**, 420-435.
86. T. Nakagawa, N. S. Bjorge and R. W. Murray, *J. Am. Chem. Soc.*, 2009, **131**, 15578.
87. N. Sivasankar, W. W. Weare and H. Frei, *J. Am. Chem. Soc.*, 2011, **133**, 12976-12979.
88. J. Towns, T. Cockerill, M. Dahan, I. Foster, K. Gaither, A. Grimshaw, V. Hazlewood, S. Lathrop, D. Lifka, G. D. Peterson, R. Roskies, J. R. Scott and N. Wilkins-Diehr, *Comput. Sci. Eng.*, 2014, **16**, 62-74.